Supporting Information for

Manganese Pyrosilicates as Novel Electrode Materials for Na-ion Batteries

Viktor Renman†, Mario Valvo†, Cheuk-Wai Tai‡, Cesar Pay Gómez†, Kristina Edström† and Anti Liivat†.

†Department of Chemistry – Ångström Laboratory, Ångström Advanced Battery Centre, Uppsala University, Box 538, SE-751 21 Uppsala, Sweden

‡Department of Materials and Environmental Chemistry, Stockholm University, SE-106 91 Stockholm, Sweden.

S1. Materials and methods

S1.1 Synthesis

The procedure for obtaining $Na_2Mn_2Si_2O_7$/C was carried out via an adaptation of previously described ways of synthesizing members within a closely related family of lithium-containing orthosilicates (*i.e.* Li_2MSiO_4).[1,2] First, appropriate amounts of $Mn(CH_3COO)_2 \cdot 4H_2O$ (Sigma Aldrich) and $NaCH_3COO \cdot 3H_2O$ (Sigma Aldrich) were dissolved in absolute ethanol (99.5%, Solveco). A mixture of ethanol and $Si(OC_2H_5)_4$ (tetraethylorthosilicate - TEOS, Sigma Aldrich) was then slowly added dropwise to the precursor solution under vigorous stirring. After the addition of a catalytic amount of glacial CH_3OOH (Sigma Aldrich), the solution was transferred to a Teflon-lined steel autoclave and maintained at 120 °C for hydrolysis, condensation and subsequent gelation to occur. The wet gel was recovered and dried in a convection oven at 60 °C. Subsequently, the dry amorphous xerogel was intimately mixed with sucrose via a ball milling procedure in acetone. For the preparation of an 'uncoated', carbon-free powder, this step was left out. After evaporating the acetone, the mixture was heat-treated at 650-700 °C for a variable period of 1-10 h under a steady flow of Ar (50 sccm) in order to achieve a carbon coating and to avoid possible oxidation of Mn^{2+}. The resulting fluffy black (*i.e.* carbon-coated) product was immediately transferred to an Ar-filled glovebox and stored there in a sealed vial before further characterization.

S1.2 XRD Analysis

Crystal structure analysis and sample purity evaluation were performed by means of powder X-ray diffraction (XRD) using a Bruker D8 diffractometer (CuK_α radiation) equipped with a LynxEye detector. Crystal structure refinement was performed using the Rietveld method[3] as implemented in TOPAS.[4] Ex-situ powder XRD measurements were also performed on some electrochemically cycled material in order to observe possible changes in the crystal structure due to removal of Na^+ ions. The corresponding cycled cells were disassembled and the reacted electrode material was thoroughly washed with dimethyl carbonate (DMC) to remove electrolyte residues prior to the analysis.

S1.3 Thermogravimetric analysis

Thermogravimetric analysis (TGA) was utilized to estimate the carbon content in the $Na_2Mn_2Si_2O_7$/C nanocomposite material. The measurements were performed on a TA instruments Q500 by putting an appropriate amount of powder in aluminum pans and heating the samples from room temperature (RT) to 600 °C at a rate of 5 °C min^{-1} under a constant flow of air (40 cm^3 min^{-1}).

S1.3 Morphological study

The morphology of the synthesized powder was observed using a high-resolution scanning electron microscope (HRSEM LEO 1550) using a dedicated In-lens detector for the secondary electrons. Transmission electron microscopy (TEM) images were collected using a field-emission electron microscope (JEOL JEM-2100F) operated at 200 kV and equipped with a Gatan Ultrascan 1000 CCD camera. TEM samples were prepared by carefully placing the powder onto a copper grid (*i.e.* supporting a holey carbon film) under inert atmosphere in an Ar-filled glove-box. The grid was then transferred from the glove-box to the microscope column by using a dedicated JEOL vacuum-transfer holder. High-resolution transmission electron microscopy (HRTEM) was carried out to study in depth the morphological, structural and textural features of the $Na_2Mn_2Si_2O_7$/C nano-composite.

S1.4 FT-IR and Raman analysis

Fourier Transform Infrared (FT-IR) measurements were performed using a Perkin-Elmer (Spectrum One) spectrometer equipped with an attenuated total reflectance (ATR) instrument. The resulting spectra were collected in a spectral range spanning from 600 to 4000 cm^{-1} with a resolution of 4 cm^{-1}. Twenty consecutive scans were run to acquire each spectrum with a good signal-to-noise (S/N) ratio.

Raman spectra were attained with a Renishaw InVia spectrometer using an excitation wavelength of 532 nm produced by a solid-state laser (Renishaw). The laser beam was focused on the surface of the specimens through a 50× objective and an initial calibration was run before the measurements using a Si wafer as a standard reference to achieve a characteristic peak located at 520.6 cm^{-1}. Thirty cumulative acquisitions with a measuring time of 60 s were collected between 200 and 1800 cm^{-1} for each spectrum to enhance the S/N ratio. A low nominal laser power of 0.5 mW was used in all the analyses together with a minimization of the beam exposure time for the samples in between subsequent scans to prevent possible degradation of their surfaces during the measurements.

S1.5 Electrode preparation and electrochemical characterization

Electrochemical characterization was carried out using composite electrodes assembled in a pouch cell configuration. The active material, $Na_2Mn_2Si_2O_7$/C, was ball-milled with carbon black (Super P, Timcal) and polyvinylidene fluoride (PVdF, Solef 5130) in a weight ratio of 80:10:10 using NMP (N-methyl-2-pyrrolidone) as solvent for the PVdF binder. The viscous slurry was spread onto an aluminium foil using a weighted wire-wound rod via a coating apparatus (KR – K Control Coater). After evaporating the solvent, circular electrodes were punched out and subsequently dried over night at 120 °C in a vacuum oven inside an Ar-filled glovebox. The electrode coatings typically had a thickness of 35-40 μm with a mass loading of 3-4 mg cm^{-2}. For the electrochemical tests, Na half-cells were assembled. The electrode stacks consisting of the prepared positive electrodes, a glass fiber separator soaked in electrolyte and a pin-rolled circular Na metal disk (serving as a combined counter- and reference electrode) were vacuum-sealed within a polymer-aluminium-polymer laminate pouch cell. The electrolyte used was 1 M $NaPF_6$ dissolved in a EC:DEC 1:1 mixture. Galvanostatic (*i.e.* constant current) experiments were carried out using an Arbin battery tester (BT2000) at room temperature (RT). OCV of the uncoated powder specimen (≈10 mg) was recorded in a Swagelok-type Na half-cell using the same electrolyte.

S1.6 DFT Calculations

An experimentally available unit cell (SG: $P2_1/n$) containing four formula units (f.u.) of $Na_2Mn_2Si_2O_7$ (*Table S2*) was used as a starting model for the calculations. The cell geometry of half-desodiated structures, with Na1 or Na2 sites only occupied, and fully desodiated model were optimised for structural analysis and calculation of desodiation potentials. DFT calculations were done using Projector-Augmented Wave (PAW) method[5] using the periodic plane-wave program VASP.[6] The PAW projection potentials "Na_sv_GW" (2s2p3s), "Mn_sv_GW" (3p4s3d), "Si_GW" (s2p2), "O_GW" (s2p4) for Na, Mn, Si and O, respectively were used from the set "potpaw_PBE.54". A Generalised Gradient Approximation (GGA) using the Perdew-Burke-Ernzerhof (PBE)[7] functional with the rotationally invariant Hubbard correction applied to Mn *d*-band was applied; for the latter, the effective parameter value of U=4 eV was adopted, which gives a more realistic *d*-electron localisation leading to a better reproduction of the experimentally measured M^{2+}/M^{3+} redox potentials.[8] The electron structure was converged with a high-spin antiferromagnetic spin configuration for Mn, since it gave slightly (≈20meV/f.u.) lower energy than the ferromagnetic one. The atomic positions and cell parameters were relaxed and optimized using conjugate gradient with the energy and force convergence criteria 0.001 eV and 0.01 eV/Å, respectively. The upper cut-off of 539 eV was chosen for the wavefunction expansion over plane waves and a 2x1x3 gamma-point centered k-mesh for Brillouin zone sampling was employed.

S1.7 Electron paramagnetic resonance (EPR)

In order to confirm the presence of Mn^{2+} in the as-prepared material, electron paramagnetic resonance (EPR) was carried out. The EPR spectra were collected at a frequency of 9.77 GHz at room temperature (RT) as the first derivative of the absorption signal using a Bruker Biospin ELEXSYS 580 spectrometer with a standard ER4102ST resonator cavity.

S1.8 Bond Valence Sum (BVS) calculations

Preferred Na-ion migration pathways are visualised through 3D mapping of the Na-ion positions in the unit cell of $Na_2Mn_2Si_2O_7$ (using VESTA software) where the deviation of Bond Valence Sum (BVS), $\Delta BVS = |BVS_{position} - BVS_{Na\text{-}O}|$, is small to predict near optimal Na-O bonding situation[9]. $BVS_{Na\text{-}O}$ is an empirical parameter for stable Na-O bonding configuration and $BVS_{position}$ is calculated at any position within the unit cell. BVS calculations we done using PyAbstantia tool[10] and visualisation using VESTA program[11].

S2. Supplementary results

S2.1 Crystallographic information on pristine $Na_2Mn_2Si_2O_7$

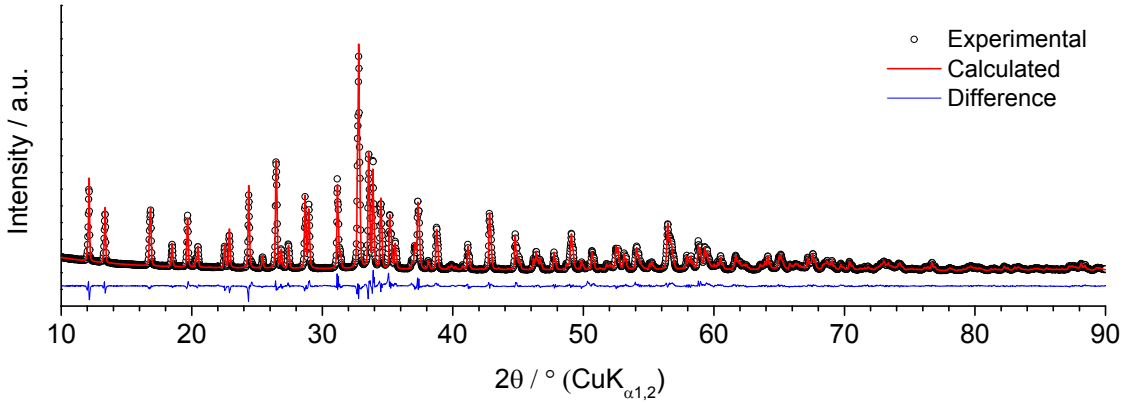

Figure S1. Experimental *X*-ray diffractogram of the as-synthesized pristine "carbon-free" $Na_2Mn_2Si_2O_7$ shown as black open circles. The calculated diffractogram is shown instead as a red line. The difference between the observed and calculated data is represented by a solid blue line.

Table S1. Fractional atomic coordinates and parameters of the refined structural model in space group no. 14 setting $P2_1/n$. The lattice parameters of the monoclinic unit cell are a=8.76382(15)Å, b= 13.29311(21) Å, c= 5.744579(90) Å, $\alpha=\gamma$=90° and β=89.8984(14)°.

Site	Np	x	y	z	Occ.	B_{eq}
Mn1	4	0.70751(31)	0.00744(22)	0.13799(56)	1	1
Mn2	4	0.11684(36)	0.08206(21)	0.33659(50)	1	1
Si1	4	0.02950(60)	0.87970(38)	0.1783(10)	1	1
Si2	4	0.45119(63)	0.16664(37)	0.1850(10)	1	1
Na1	4	0.29830(83)	0.24763(58)	0.7257(12)	1	1
Na2	4	0.61559(84)	0.15858(44)	0.6736(13)	1	1
O1	4	0.9556(11)	0.21161(61)	0.6246(17)	1	1
O2	4	0.0930(11)	0.04077(63)	0.7050(15)	1	1
O3	4	0.6092(13)	0.13444(73)	0.2867(17)	1	1
O4	4	0.0251(12)	0.16722(66)	0.0645(16)	1	1
O5	4	0.3306(11)	0.15345(58)	0.3799(17)	1	1
O6	4	0.8028(10)	0.06242(62)	0.8166(16)	1	1
O7	4	0.4155(10)	0.11801(59)	0.9397(16)	1	1

Numbers in parenthesis are estimated standard deviations. R_p=6.54, R_{wp}=8.91, χ^2=11.92.

S2.2 Crystallographic information on carbon-coated $Na_2Mn_2Si_2O_7$

Table S2. Fractional atomic coordinates and parameters of the refined structural model in space group no. 14 setting $P2_1/n$. The lattice parameters of the monoclinic unit cell are a= 8.78031(44) Å, b= 13.29189(62) Å, c= 5.74355(24) Å, $\alpha=\gamma=90°$ and β= 90.1351(56)°.

Site	Np	x	y	z	Occ.	B_{eq}
Mn1	4	0.70823(38)	0.00710(29)	0.14271(68)	1	1
Mn2	4	0.11788(46)	0.08143(28)	0.34077(59)	1	1
Si1	4	0.02868(77)	0.88230(42)	0.1692(12)	1	1
Si2	4	0.45036(70)	0.16642(45)	0.1948(13)	1	1
Na1	4	0.2977(10)	0.25158(73)	0.7306(15)	1	1
Na2	4	0.6052(10)	0.15674(56)	0.6745(18)	1	1
O1	4	0.9642(13)	0.21620(73)	0.6170(22)	1	1
O2	4	0.0919(14)	0.05287(77)	0.7026(18)	1	1
O3	4	0.6095(16)	0.13079(88)	0.2753(22)	1	1
O4	4	0.0186(18)	0.16171(83)	0.0560(20)	1	1
O5	4	0.3346(15)	0.15060(66)	0.3775(20)	1	1
O6	4	0.8095(15)	0.06281(83)	0.8074(21)	1	1
O7	4	0.4113(16)	0.11383(68)	0.9406(23)	1	1

Numbers in parenthesis are estimated standard deviations. R_p=3.87, R_{wp}=5.00, χ^2=3.73

S2.3 Ex-situ XRD comparison with simulated models

In order to investigate which desodiation pathway is more likely, an ex-situ XRD experiment was conducted. The experimentally obtained diffraction pattern of a sample desodiated at 4.2 V *vs.* Na^+/Na is shown in Figure S2b. By a comparison with the two possible desodiation models obtained from the DFT calculations (Fig. S2c-f), it becomes evident that one of the simulated patterns shows more similarities with the experimental data. The most striking similarity appears with regards to the shift in position and intensity of the (110) and (020) peaks, respectively. Hence, it is suggested that the most probable desodiation pathway is one in which sodium is preferentially removed from the Na1 site, while the Na2 site remains occupied. The remaining discrepancies between the experimental (Fig S2b) and the model patterns (Fig S2d-f) beyond the first three peaks could be attributed to lattice strain and disorder in site occupation. For example, for the model (d) in Fig S2, a monoclinic distortion would shift (101) reflection to the opposite (lower) angle than for the other models (see the change in β in Fig. S7). Such situation is also consistent with the distortion and broadening of the peaks in the experimental pattern of the desodiated phase (Fig. S2b). Note that the change in average cell parameters estimated from the Le Bail fit (Fig S7d) are in line with the above interpretation, including the modest decrease in the average unit cell volume: ~3.2% on extraction of ~ 1 Na per formula unit.

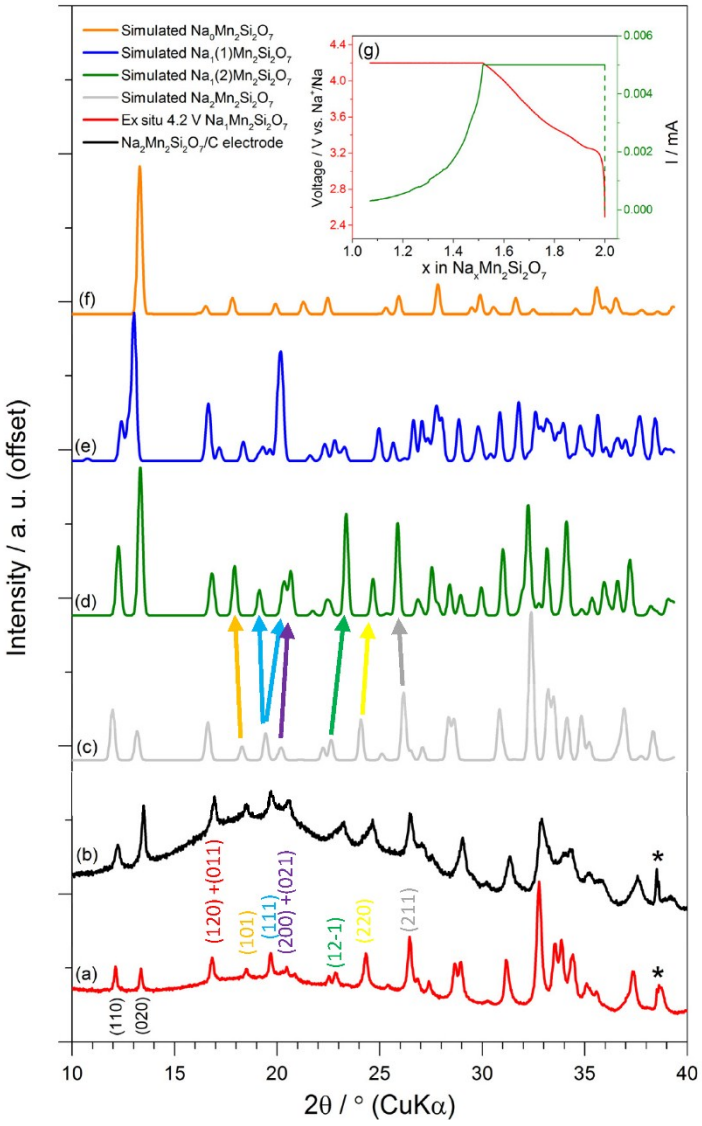

Figure S2. (a) Experimental XRD pattern of the as-prepared $Na_2Mn_2Si_2O_7$/C sample. (b) Experimental XRD pattern of material subjected to galvanostatic charging up to 4.2 V *vs.* Na^+/Na followed by a constant potential step at 4.2 V. Simulated XRD patterns derived from DFT calculations for a sodiated (c), a partially desodiated model in which the Na2 site is still occupied (d), a partially desodiated model in which the Na1 site is still occupied (e), and a fully desodiated compound (f). The charging curve corresponding to the experimentally desodiated sample is show in the inset (g). The reflections for low angle peaks are also shown. Beyond the first three peaks, the arrows indicate the correspondence between reflections (color coded) of the sodiated (c) and one of the desodiated model (d).

S2.3 Thermogravimetric analysis

The C-coated sample displays a significant loss of mass in the temperature range of 260-360 °C closely followed by an increase in mass, as marked by the red line in Fig. S3. The carbon-free sample is stable in air at temperatures up to 360 °C, after which a mass increase is observed, as indicated by the black trace in Fig. S3. By comparing the two thermogravimetric curves obtained from the two different samples, the carbon-content of the coated sample can be estimated with relative ease, since the combustion of carbon (*i.e.* mass-loss) and oxidation of the pristine material in air (mass-gain) clearly take place at separate temperature intervals. We thus estimate the amount of conductive carbon in the $Na_2Mn_2Si_2O_7$/C nanocomposite to be approximately 13 % by weight.

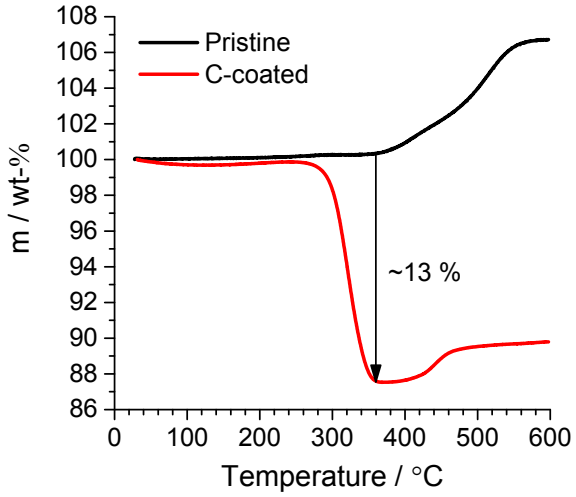

Figure S3. Thermogravimetric plots comparing carbon-coated and pristine $Na_2Mn_2Si_2O_7$ exposed to progressive oxidation in the temperature range of RT-600 °C at a heating rate of 5 °C min^{-1} in air.

S2.4 Raman and FT-IR analyses

The small band around 590 cm^{-1} in Fig. 2a could tentatively be associated with Mn–O lattice vibrations[12,13] of the tetrahedral $[MnO_4]^{-6}$ units here, whereas the other weak bands between 550 and 400 cm^{-1} can be assigned to Si–O–Si bending modes.[14] The contribution from the orthosilicate impurities found from the Rietveld refinement (≈5% range) are unlikely to be resolved here; Also the presence of other possible relevant phases like Na_2SiO_3 (Raman peaks at 589 and 986 cm^{-1})[15] or Na_2CO_3 (main IR peaks around 863 cm^{-1} and 1450 cm^{-1})[16] is not found in any significant proportion here. Furthermore, it was found that the title compound is not really reactive in terms of deterioration of its surface properties via both IR and Raman analyses of aged material which had been exposed to ambient conditions for a prolonged period of time (>24 h).

A brief summary of the main features related to the D and G bands for the pristine $Na_2Mn_2Si_2O_7$ and $Na_2Mn_2Si_2O_7$/C specimens can be found in Table S3.

Table S3. Comparative table of the main features extracted from Raman analyses on the samples.

Sample properties	ν_D *[cm^{-1}]*	ν_G *[cm^{-1}]*	I_D/I_G ratio	L_a *[nm]*
Pristine	1367	1603	0.687	1.12
C-coated	1345	1594	0.870	1.26

$L_a=[(I_D/I_G)/C'(\lambda)]^{1/2}$, where C' is a constant at a fixed □ with the dimensions of [$Å^{-2}$]

This formula is allowed, as the carbon found in the surface of these samples is mostly amorphous with typical graphene cluster size <20 Å (see A.C. Ferrari[17]).

S2.5 SEM and TEM analyses

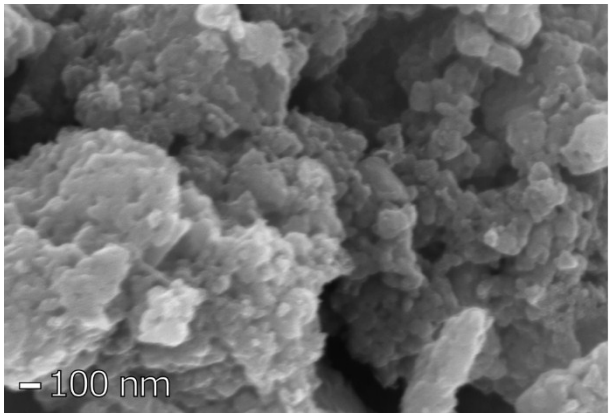

Figure S4. SEM micrograph of carbon-coated $Na_2Mn_2Si_2O_7$ obtained at 700 °C under Ar-flow displaying the microscopic morphology of the product.

Analysis of the TEM micrographs was conducted with the aid of the ImageJ package.[18] Obstacles related to the non-ideal sample morphology, i.e. non-flatness, carbon coating, as well as instrumental limitations were mainly addressed by Fast Fourier Transform (FFT) of selected regions of interest, as displayed in Fig. S5.

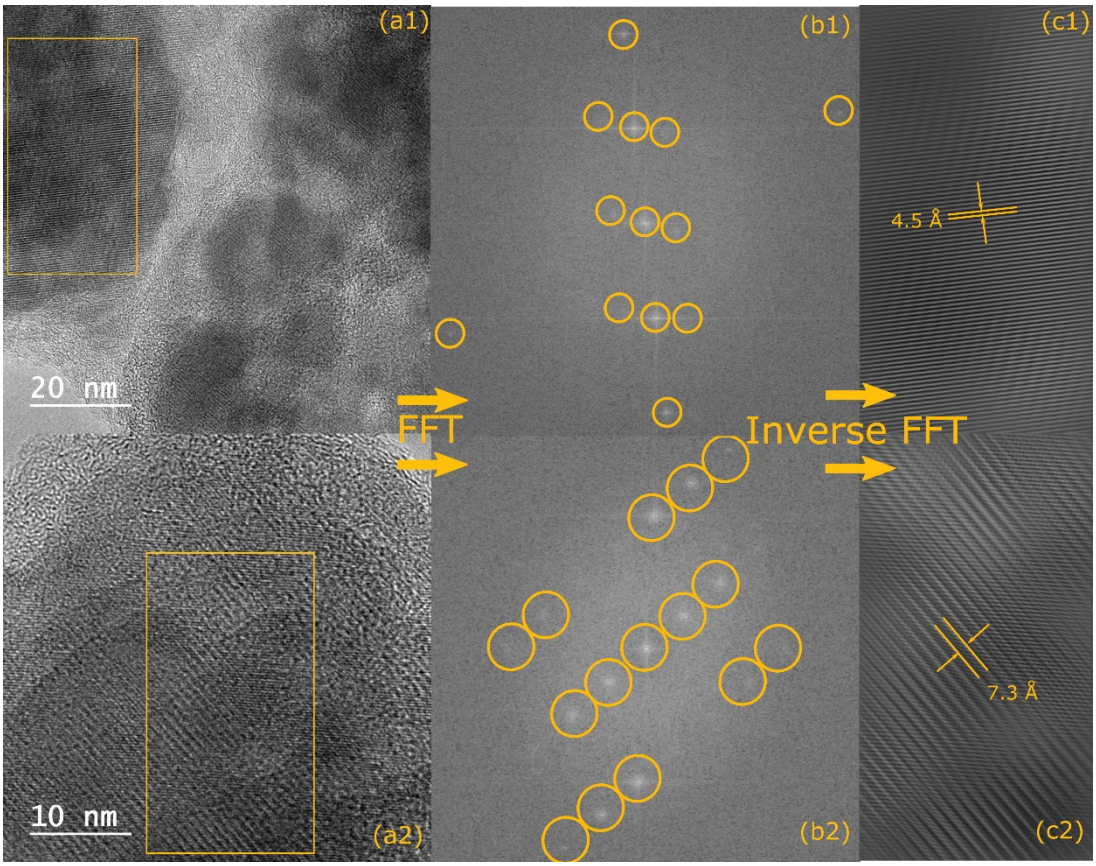

Figure S5. HRTEM images of $Na_2Mn_2Si_2O_7$/C taken at two different sample spots (a1-2) displaying characteristic lattice fringes. The rectangular selections highlight areas of interest that were subjected to a Fast Fourier Transform (FFT) routine. The resulting spots in reciprocal space are highlighted using circles (b1-2). By considering only the encircled spots and reverting to real space via an inverse FFT, the appearance of the distinctive *d*-spacings is greatly enhanced (c1-2).

S.2.6 Electron paramagnetic resonance

An experimental EPR spectrum of a carbon coated $Na_2Mn_2Si_2O_7$ sample is shown in Fig. S6 and its profile displays a single Lorentzian line. This suggests that the signal originates from a dense phase with short Mn-Mn distance as in inorganic oxides, in which the fine structure of the spectrum is not resolvable. Since the spectrum is entirely dominated by the $m_s = +1/2 \leftrightarrow -1/2$ transition with a *g* value of 2.01 at 347.92 mT, we consider these findings as evidence for the presence of Mn^{2+} in structural sites having close to cubic symmetry - in line with other previous observations[19,20] and structural XRD analysis.

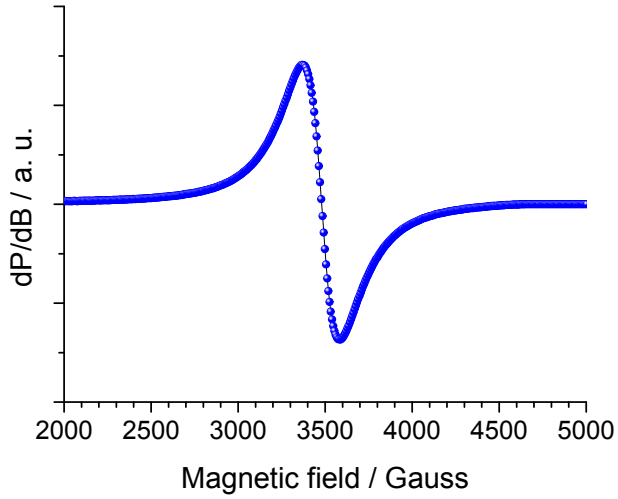

Figure S6. EPR spectrum of pristine $Na_2Mn_2Si_2O_7$ recorded at room temperature at 2 mW microwave power and a modulation amplitude of 1 Gauss.

S.2.7 DFT calculations

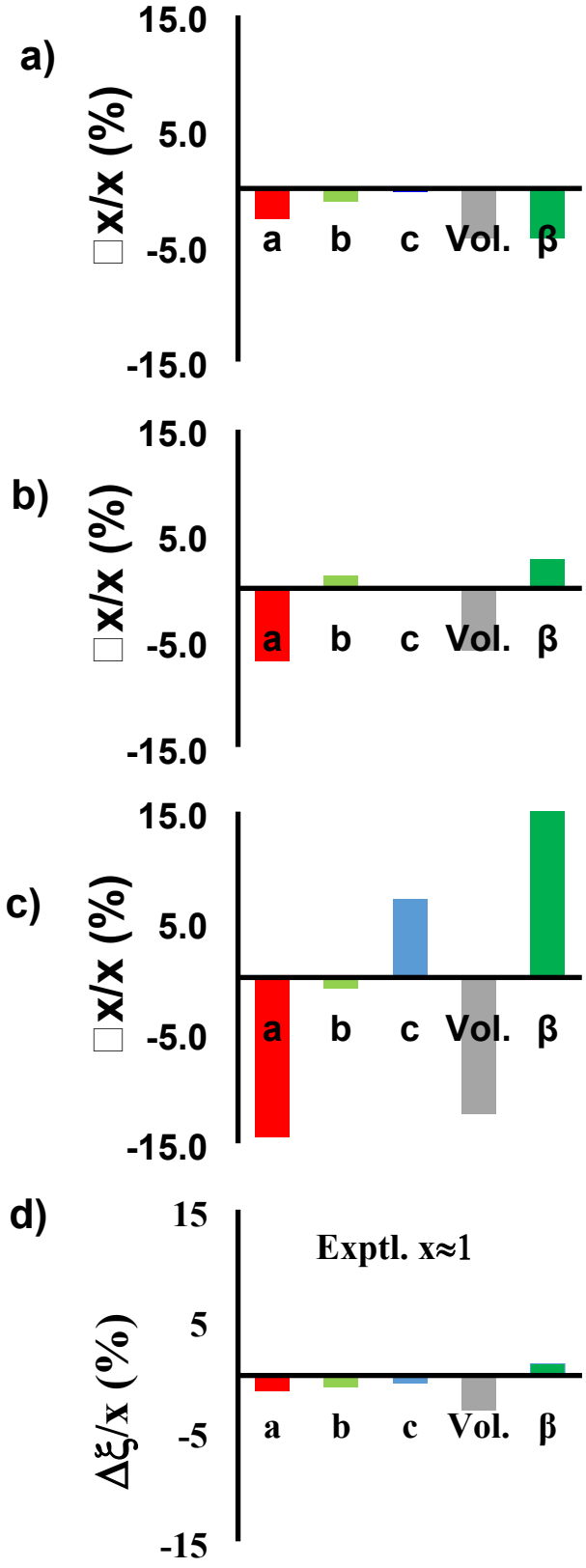

Figure S7. Relative changes in cell parameters, cell volume and angle β upon desodiation of $Na_2Mn_2Si_2O_7$ for the models with only Na2 site occupied (a), Na1 site occupied (b) and for the completely desodiated structure (c) with respect to the parameters of the initial, fully sodiated structure. The corresponding changes from the experimental data (Fig. S2) are also shown for comparison (d).

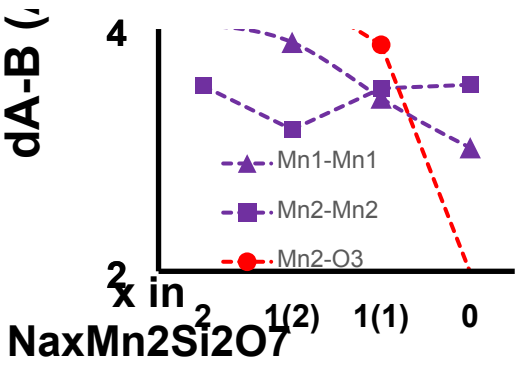

Figure S8. Key distances within the structure of $Na_2Mn_2Si_2O_7$ (2) upon desodiation for the models with only Na2 site occupied (1(2)), Na1 site occupied (1(1)) and for the completely desodiated structure (0).

S.2.8 Bond Valence Sum (BVS)

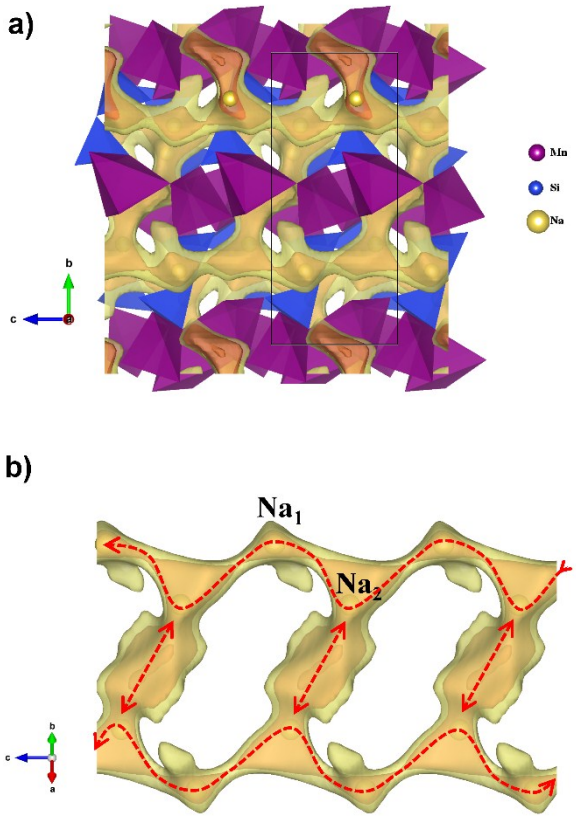

Figure S9. The isosurface corresponding to two different deviations for Na Bond Valence Sum (BVS), ΔBVS <0.15 (orange) and ΔBVS <0.3 (yellow) from its optimal value are shown together with the structure of $Na_2Mn_2Si_2O_7$ (a) and in magnification without the structure (b). Na-ion positions and the preferred Na-ion migration pathways (red arrows) are highlighted.

References

(1) Li, Y.-X.; Gong, Z.-L.; Yang, Y. Synthesis and Characterization of Li2MnSiO4/C Nanocomposite Cathode Material for Lithium Ion Batteries. *J. Power Sources* **2007**, *174* (2), 528–532.

(2) Gong, Z. L.; Li, Y. X.; He, G. N.; Li, J.; Yang, Y. Nanostructured Li2FeSiO4 Electrode Material Synthesized through Hydrothermal-Assisted Sol-Gel Process. *Electrochem. Solid-State Lett.* **2008**, *11* (5), A60.

(3) Rietveld, H. M. A Profile Refinement Method for Nuclear and Magnetic Structures. *J. Appl. Crystallogr.* **1969**, *2*, 65–71.

(4) Coelho, A. A. TOPAS. *Topas*. Coelho Software: Brisbane, Australia.

(5) Blöchl, P. E. Projector Augmented-Wave Method. *Phys. Rev. B* **1994**, *50* (24), 17953–17979.

(6) Kresse, G.; Furthmüller, J. Efficient Iterative Schemes for Ab Initio Total-Energy Calculations Using a Plane-Wave Basis Set. *Phys. Rev. B* **1996**, *54* (16), 11169–11186.

(7) Perdew, J. P.; Burke, K.; Ernzerhof, M. Generalized Gradient Approximation Made Simple. *Phys. Rev. Lett.* **1996**, *77* (18), 3865–3868.

(8) Arroyo-de Dompablo, M. E.; Armand, M.; Tarascon, J. M.; Amador, U. On-Demand Design of Polyoxianionic Cathode Materials Based on Electronegativity Correlations: An Exploration of the Li2MSiO4 System (M=Fe, Mn, Co, Ni). *Electrochem. commun.* **2006**, *8* (8), 1292–1298.

(9) Adams, S. Relationship between Bond Valence and Bond Softness of Alkali Halides and Chalcogenides. *Acta Crystallogr. Sect. B Struct. Sci.* **2001**, *57* (3), 278–287.

(10) Nishimura, S. PyAbstantia, 2017. http://shinichinishimura.github.io/pyabst/

(11) Momma, K.; Izumi, F. VESTA: A Three-Dimensional Visualization System for Electronic and Structural Analysis. *J. Appl. Crystallogr.* **2008**, *41* (3), 653–658.

(12) Gosztola, D.; Weaver, M. J. Electroinduced Structural Changes in Manganese Dioxide + Manganese Hydroxide Films as Characterized by Real-Time Surface-Enhanced Raman Spectroscopy. *J. Electroanal. Chem. Interfacial Electrochem.* **1989**, *271* (1–2), 141–154.

(13) Buciuman, F.; Patcas, F.; Craciun, R.; Zahn, D. R. T. Vibrational Spectroscopy of Bulk and Supported Manganese Oxides. *Phys. Chem. Chem. Phys.* **1999**, *1* (1), 185–190.

(14) Wierzbicka-Wieczorek, M.; Kolitsch, U.; Tillmanns, E. The Crystal Structures of Three New Complex Silicates of Scandium. *Can. Mineral.* **2010**, *48*, 51–68.

(15) Richet, P.; Mysen, B.; Andrault, D. Melting and Premelting of Silicates: Raman Spectroscopy and X-Ray Diffraction of Li2SiO3 and Na2SiO3. *Phys. Chem. Miner.* **1996**, *23* (3), 157–172.

(16) Doubaji, S.; Valvo, M.; Saadoune, I.; Dahbi, M.; Edström, K. Synthesis and Characterization of a New Layered Cathode Material for Sodium Ion Batteries. *J. Power Sources* **2014**, *266*, 275–281.

(17) Ferrari, A. C.; Robertson, J. Interpretation of Raman Spectra of Disordered and Amorphous Carbon. *Phys. Rev. B* **2000**, *61* (20), 14095–14107.

(18) Schneider, C. A.; Rasband, W. S.; Eliceiri, K. W. NIH Image to ImageJ: 25 Years of Image Analysis. *Nat. Methods* **2012**, *9* (7), 671–675.

(19) Aravindan, V.; Karthikeyan, K.; Ravi, S.; Amaresh, S.; Kim, W. S.; Lee, Y. S. Adipic Acid Assisted Sol–gel Synthesis of Li2MnSiO4 Nanoparticles with Improved Lithium Storage Properties. *J. Mater. Chem.* **2010**, *20* (35), 7340.

(20) Koleva, V.; Zhecheva, E.; Stoyanova, R. Facile Synthesis of LiMnPO4 Olivines with a Plate-like Morphology from a Dittmarite-Type KMnPO4·H2O Precursor. *Dalt. Trans.* **2011**, *40* (28), 7385.